Monthly Notices of the ROYAL ASTRONOMICAL SOCIETY

MNRAS **513,** 5076–5087 (2022) https://doi.org/10.1093/mnras/stac1221
Advance Access publication 2022 May 03

The SAMI Galaxy Survey: the link between [α/Fe] and kinematic morphology

Peter J. Watson [1★] Roger L. Davies,[1] Jesse van de Sande [2,3] Sarah Brough [2,4] Scott M. Croom [2,3] Francesco D'Eugenio [5,6] Karl Glazebrook,[2,7] Brent Groves,[8] Ángel R. López-Sánchez,[2,9,10] Nicholas Scott,[2,3] Sam P. Vaughan [3] C. Jakob Walcher,[11] Joss Bland-Hawthorn [3] Julia J. Bryant,[2,3,12] Michael Goodwin,[9] Jon S. Lawrence,[13] Nuria P. F. Lorente,[9] Matt S. Owers [2,10,14] and Samuel Richards[15]

[1]*Sub-Department of Astrophysics, Department of Physics, University of Oxford, Denys Wilkinson Building, Keble Rd., Oxford OX1 3RH, UK*
[2]*ARC Centre of Excellence for All Sky Astrophysics in 3 Dimensions (ASTRO 3D) , Canberra, ACT 2601, Australia*
[3]*Sydney Institute for Astronomy (SIfA), School of Physics, University of Sydney, NSW 2006, Australia*
[4]*School of Physics, University of New South Wales, NSW 2052, Australia*
[5]*Cavendish Laboratory and Kavli Institute for Cosmology, University of Cambridge, Madingley Rise, Cambridge, CB3 0HA, UK*
[6]*Sterrenkundig Observatorium, Universiteit Gent, Krijgslaan 281 S9, B-9000 Gent, Belgium*
[7]*Centre for Astrophysics & Supercomputing, Swinburne University of Technology, Victoria 3122, Australia*
[8]*Research School of Astronomy & Astrophysics, Australian National University, Mt Stromlo Observatory, Cotter Rd, Weston Creek, ACT 2611, Australia*
[9]*Australian Astronomical Optics, Macquarie University, 105 Delhi Rd, North Ryde, NSW 2113, Australia*
[10]*Department of Physics and Astronomy, Macquarie University, NSW 2109, Australia*
[11]*Leibniz-Institut für Astrophysik Potsdam (AIP), An der Sternwarte 16, D-14482 Potsdam, Germany*
[12]*Australian Astronomical Optics, AAO-USydney, School of Physics, Building A28, University of Sydney, NSW 2006, Australia*
[13]*Australian Astronomical Optics - Macquarie, Macquarie University, NSW 2109, Australia*
[14]*Astronomy, Astrophysics and Astrophotonics Research Centre, Macquarie University, Sydney, NSW 2109, Australia*
[15]*SOFIA Science Center, USRA, NASA Ames Research Center, Building N232, M/S 232-12, P.O. Box 1, Moffett Field, CA 94035-0001, USA*

Accepted 2022 April 26. Received 2022 April 25; in original form 2022 March 4

ABSTRACT

We explore a sample of 1492 galaxies with measurements of the mean stellar population properties and the spin parameter proxy, λ_{R_e}, drawn from the SAMI Galaxy Survey. We fit a global [α/Fe]–σ relation, finding that $[\alpha/\mathrm{Fe}] = (0.395 \pm 0.010)\log_{10}(\sigma) - (0.627 \pm 0.002)$. We observe an anti-correlation between the residuals $\Delta[\alpha/\mathrm{Fe}]$ and the inclination-corrected $\lambda^{\mathrm{eo}}_{R_e}$, which can be expressed as $\Delta[\alpha/\mathrm{Fe}] = (-0.057 \pm 0.008)\lambda^{\mathrm{eo}}_{R_e} + (0.020 \pm 0.003)$. The anti-correlation appears to be driven by star-forming galaxies, with a gradient of $\Delta[\alpha/\mathrm{Fe}] \sim (-0.121 \pm 0.015)\lambda^{\mathrm{eo}}_{R_e}$, although a weak relationship persists for the subsample of galaxies for which star formation has been quenched. We take this to be confirmation that disc-dominated galaxies have an extended duration of star formation. At a reference velocity dispersion of 200 km s^{-1}, we estimate an increase in half-mass formation time from ∼0.5 Gyr to ∼1.2 Gyr from low- to high-$\lambda^{\mathrm{eo}}_{R_e}$ galaxies. Slow rotators do not appear to fit these trends. Their residual α-enhancement is indistinguishable from other galaxies with $\lambda^{\mathrm{eo}}_{R_e} \lessapprox 0.4$, despite being both larger and more massive. This result shows that galaxies with $\lambda^{\mathrm{eo}}_{R_e} \lessapprox 0.4$ experience a similar range of star formation histories, despite their different physical structure and angular momentum.

Key words: galaxies: evolution – galaxies: formation – galaxies: kinematics and dynamics – galaxies: stellar content.

1 INTRODUCTION

1.1 Background

Understanding the formation history of individual galaxies requires both observations and modelling of their physical properties in three dimensions. Even in the era of large spectroscopic surveys we are limited by only being able to observe galaxies at a single point in their evolution.

One vital tool is that of stellar population analysis, which gives us an insight into the time-scales and assembly history of the stellar component of galaxies. Through comparison with semi-empirical and theoretical models, we can determine integrated properties such as the light-weighted age, metallicity, and elemental abundances. Many models eschew the vast computational cost of calculating individual elemental abundances by grouping together elements with a similar formation mechanism. Assuming that the quantity of these elements produced can be directly correlated to the number of supernovae of a given type, this significantly limits the number of free parameters. The α-element abundance is one of the most commonly utilized groupings. These elements are predominantly formed in massive stars, prior to being ejected through core-collapse

★ E-mail: peter.watson2@physics.ox.ac.uk

supernovae. The [α/Fe] ratio compares the abundance of α-elements to Fe, which is mainly formed over considerably longer time-scales in Type Ia supernovae. This abundance ratio therefore measures the relative contribution of each type of supernovae to the ISM, or more precisely, to the integrated light from stars that have formed from the ISM. Over a longer period of star formation, the relative contribution from Type Ia supernovae becomes more significant, and so [α/Fe] will tend towards solar values (Greggio & Renzini 1983). For galaxies that are no longer actively forming stars, this measure therefore reflects the total duration of star formation prior to quenching (de La Rosa et al. 2011).

We can also determine the dynamical properties of a galaxy using stellar template libraries. This particular field has a long and detailed history, dating back to the first discovery of 'nebular rotation' (Slipher 1914). More recently, with the advent of integral field spectroscopy, the SAURON (de Zeeuw et al. 2002) and ATLAS^{3D} (Cappellari et al. 2011) surveys enabled a quantitative classification of galaxies based on their kinematics. Based on features in the velocity field (Krajnović et al. 2011), galaxies were separated into fast rotators (FRs), with ordered rotation and discs, and slow rotators (SRs), with more complex velocity fields (Emsellem et al. 2011). The selection criteria have since been refined (Cappellari 2016; van de Sande et al. 2021a), but the presence of a distinct bimodality in the kinematic distribution of galaxies has remained (Graham et al. 2018), suggesting multiple formation scenarios.

There have been many studies whose motivation has been to investigate the build-up of mass and angular momentum, in order to better understand the origin of present-day morphologies (Naab et al. 2014, contains a thorough review). There are, however, fewer studies linking galaxy kinematics and elemental abundance ratios. Eggen, Lynden–Bell & Sandage (1962) investigated the motion of stars within the Milky Way, finding an anti-correlation between the ellipticity of an orbit and the inferred stellar metallicity. They utilized this result in a model galaxy to estimate the formation time-scale, providing one of the first links between stellar dynamics and stellar properties.

Franx & Illingworth (1990) made the assumption that colour differences within and between galaxies were due only to changes in the stellar metallicity, and found a correlation between this inferred metallicity, and the local escape velocity. This was confirmed by Davies, Sadler & Peletier (1993), using a spectroscopic measurement of metallicity, alongside the observation that the line indices Mg_2 and ⟨Fe⟩ coupled differently to the galaxy kinematics. Trager et al. (2000) followed on from this with their findings of a simple scaling relation between the stellar velocity dispersion σ of early-type galaxies (ETGs), and the abundance ratio [α/Fe]. More recently, studies such as McDermid et al. (2015, hereafter: M15) have focused on the internal kinematics of ETGs, and have shown that non-regularly rotating galaxies are offset to lower metallicities compared to the global mass–metallicity relation.

Here, we focus primarily on the [α/Fe]–σ relation. Since its initial discovery, it has proven to be a useful test for simulations and semi-analytic models of galaxy formation, despite some difficulties in reproducing this relation across different mass scales (Segers et al. 2016). Whilst comparisons across size, optical morphology, and environment are well researched (*e.g.* Annibali et al. 2011; Scott et al. 2017; Sánchez et al. 2021; Watson et al. 2022), the α-enhancement as a function of galactic dynamics has not been investigated as thoroughly.

In M15, the authors also looked at offsets from a global [α/Fe]–σ relation, using the regular/non-regular rotator classification from Krajnović et al. (2011). Here, using a sample of 260 ETGs, they found no measurable difference between the two kinematic classes. Bernardi et al. (2019, hereafter: B19), after stacking spectra from elliptical galaxies in the SDSS-IV MaNGA survey (Bundy et al. 2015), instead found SRs were α-enhanced by 0.04 dex. However, they also used a different selection criteria to Cappellari (2016), in order to prevent contamination of their FR sample, which may have the unintended effect of obscuring or altering any underlying trends. Krajnović et al. (2020) briefly touched on the [α/Fe]–σ relation, but showed no obvious difference in the residuals Δ[α/Fe] between FRs and SRs.

Perhaps the greatest limitation on these previous studies has been the morphological selection, with many only investigating ETGs. Considering later morphological types, we note that substantial number of spiral and lenticular galaxies can be separated out into two distinct components, a central bulge, and an extended disc. Under the inside-out scenario of galaxy formation, so-called classical bulges are thought to form through violent gas collapse or mergers (Larson 1974; Bender, Burstein & Faber 1992) over short time-scales, with the disc gradually building up around them. In this scenario, disc-dominated galaxies will have had a longer overall duration of star formation relative to bulge-dominated galaxies, and show a greater degree of rotational support. We can therefore use [α/Fe] as an indicator of the duration of star formation, and λ_{R_e} as a measure of the rotational support, to explore the extent to which this formation scenario is supported by the observational evidence.

In order to determine the kinematic classification, we require the full spatial information afforded by integral-field spectroscopy (IFS). There exist several large IFS surveys to date, including the CALIFA Survey (Sánchez et al. 2012), ATLAS^{3D} (Cappellari et al. 2011), and SDSS-IV MaNGA (Bundy et al. 2015). Here, we present results drawn from the SAMI (Sydney-AAO Multi-object Integral field spectrograph) Galaxy Survey (SGS, Bryant et al. 2015). In Section 2, we describe the SGS in more detail, including the sources of the ancillary data used. The methods used for extracting both the luminosity-weighted stellar population parameters and the kinematics are summarized in Section 3. We present our results, the dependence of [α/Fe] on the dynamical properties of galaxies in 4. Finally, we discuss the implications of our research and conclude in Sections 5 and 6. In line with other SAMI team papers, we assume a ΛCDM cosmology, with $\Omega_m = 0.3$, $\Omega_\Lambda = 0.7$, and $H_0 = 70\,km\,s^{-1}Mpc^{-1}$. All magnitudes given are in the AB system (Oke & Gunn 1983), and stellar masses and star-formation rates (SFRs) assume the initial mass function of Chabrier (2003).

2 DATA

2.1 SAMI Galaxy Survey

The SAMI instrument and survey design are detailed extensively in both Croom et al. (2012) and Bryant et al. (2015). The instrument comprises 13 Integral Field Units (IFUs, also known as *hexabundles* in SAMI), which can be deployed over a 1-degree diameter field of view, each with an individual field of view of 15 arcsec (Bland-Hawthorn et al. 2011; Bryant et al. 2014). The IFUs are mounted at the prime focus of the Anglo-Australian Telescope (AAT), and each consists of 61 individual fibres. Observations are dithered to create data cubes with a 0.5-arcsec spaxel size. All 819 fibres (including 26 allocated to blank sky observations for calibration purposes) are fed into the AAOmega spectrograph (Saunders et al. 2004; Smith et al. 2004; Sharp et al. 2006). This is composed of a blue arm, with spectral resolution $R \sim 1800$ over the wavelength range 3750–

5750 Å, and a higher resolution red arm, with wavelength coverage 6300–7400 Å and $R \sim 4300$ (van de Sande et al. 2017b).

The SGS consists of 3426 observations of 3068 unique galaxies, available as part of the SAMI public data releases (Allen et al. 2015; Green et al. 2018; Scott et al. 2018; Croom et al. 2021). The survey spans a redshift range $0.004 < z < 0.115$, and a stellar mass range $M_* \sim 10^7$ to $10^{12}\ M_\odot$. Field and group galaxies were drawn from the Galaxy And Mass Assembly (GAMA) survey (Driver et al. 2011), with the selection being volume-limited in each of four stellar mass cuts. An additional sample of cluster galaxies was drawn from the survey of eight low-redshift clusters in Owers et al. (2017), to extend the environmental sampling.

2.2 Ancillary data

We make use of additional measurements by other members of the SAMI team throughout our analysis. These include circularized effective radii (r_e), measured using the Multi Gaussian Expansion (MGE, Emsellem, Monnet & Bacon 1994) algorithm of Cappellari (2002) and photometric fits by D'Eugenio et al. (2021) to r-band images from either SDSS Data Release 9 (Ahn et al. 2012) or VST ATLAS surveys (Shanks et al. 2013, 2015). Optical morphological classifications are taken from SAMI Public Data Release 3 (Croom et al. 2021), following the method of Cortese et al. (2016), where galaxies were designated as one of four types (Ellipticals, S0s, early- and late-type spirals). This was based on visual inspection of colour images by ∼10 SAMI team members, taken from the same sources as the photometric fits. Galaxies were assigned an integer between 0 (for ellipticals) and 3 (for late-type spirals and irregulars), with half-integers reserved for galaxies where the classification was split between two morphological types.

Stellar masses are taken from the SGS sample catalogue (Bryant et al. 2015). These were derived from the rest-frame i-band absolute magnitude and $g - i$ colour by using the colour–mass relation following the method of Taylor et al. (2011). Measurements of the global SFR are taken from DR3, using the method described in Medling et al. (2018), and are based on extinction-corrected Hα fluxes, which are converted to SFRs using the relation of Kennicutt, Tamblyn & Congdon (1994).

3 METHOD

3.1 Stellar populations

Stellar population measurements are taken from Watson et al. (2022), using an approach based on measurements of absorption line indices. We briefly summarise the method here.

We utilize 20 Lick indices defined by Worthey & Ottaviani (1997) and Trager et al. (1998), which fall within the SAMI wavelength range. This comprises five Balmer lines (Hδ_A, Hδ_F, Hγ_A, Hγ_F, Hβ), six iron-dominated indices (Fe4383, Fe4531, Fe5015, Fe5270, Fe5335, Fe5406), and the molecular and elemental lines CN1, CN2, Ca4227, G4300, Ca4455, C4668, Mg1, Mg2, and Mg$_b$. The galaxies were corrected for emission-line infill and bad pixels through a three-fold fit using PPXF (Cappellari 2017), and the MILES empirical stellar spectra of Falcón–Barroso et al. (2011). The initial fit weighted all pixels equally, and the standard deviation of the residuals allowed us to determine a scaling factor for the noise spectrum. The second fit weighted pixels according to this noise spectrum, and employed a 3σ clipping method to determine bad pixels on the detector, and those contaminated by emission-line infill. For the final fit, these regions were masked out, and the resulting best-fitting output from PPXF was used to replace the missing values. This method of replacing anomalous pixels, based on emission-free template spectra, is more robust than interpolation, or subtracting fitted emission lines, particularly for low S/N spectra.

The cleaned galaxy spectra were then broadened to the required Lick/IDS resolution (Worthey & Ottaviani 1997), by convolution with a wavelength-dependent Gaussian. This convolution accounted for the instrumental resolution, and intrinsic broadening due to velocity dispersion. For galaxies and indices where the combined broadening already exceeded the Lick/IDS resolution, a correction factor was applied (see Watson et al. 2022, for further details). The indices were measured using the variance-weighted method of Cenarro et al. (2001). The errors on the indices were estimated following a bootstrap procedure, in which noise was randomly added to the galaxy spectra, and the indices remeasured. After 100 realizations, the standard deviation was taken as the error on each index.

The indices were used to predict simple stellar population (SSP) parameters using the models of Thomas et al. (2010). These models predict Lick index measurements as a function of $\log_{10}$(age), [Z/H], and [α/Fe]. The χ^2 minimization procedure of Proctor, Forbes & Beasley (2004) was utilized to find the best-fitting combination of SSP parameters. Galaxies were rejected if fewer than five indices were available, or if the indices did not include at least one Balmer index, and one Fe index. Indices were also rejected from the fit if they lay more than 1σ outside the model grid, so as not to bias the solution.

3.2 Kinematics

Measurements of the stellar velocity dispersion, σ, are taken from SAMI DR3 (Croom et al. 2021), and are measured from spectra within an r_e aperture. These values are measured following an almost identical method to that in Section 3.1, which is described in detail in van de Sande et al. (2017b). The primary difference extends from the treatment of the emission lines, which are masked out entirely for measuring the stellar kinematics. Errors are estimated following a Monte Carlo approach. The spectrum is divided into 14 regions, with residuals from the final fit randomly reallocated within each region. These residuals are added to the original galaxy spectrum, then σ can be remeasured using the best-fitting template. This process is repeated 100 times, with the standard deviation of the new measurements taken as the error on σ.

Measurements of the spin parameter proxy, λ_{R_e}, are also taken from SAMI DR3, again using a method from van de Sande et al. (2017b). These values are derived using the definition of Emsellem et al. (2007):

$$\lambda_R = \frac{\langle R|V|\rangle}{\langle R\sqrt{V^2+\sigma^2}\rangle} = \frac{\sum_{i=0}^{N_{\rm spx}} F_i R_i |V_i|}{\sum_{i=0}^{N_{\rm spx}} F_i R_i \sqrt{V_i^2+\sigma_i^2}}, \quad (1)$$

where i is the spaxel position, F_i is the flux of the $i^{\rm th}$ spaxel, and V_i and σ_i are the stellar velocity and velocity dispersion in km s^{-1}. The definition of R_i is adopted from Cortese et al. (2016), in that it is the semimajor axis of the ellipse on which each spaxel sits, as opposed to the circular projected radius as originally used by Emsellem et al. (2007). λ_{R_e} is calculated using an elliptical aperture with semimajor axis R_e, with all spaxels that pass the kinematic quality cuts Q_1 and Q_2 (van de Sande et al. 2017b). A fill factor of 95 per cent of good spaxels within the aperture is required for these measurements. When the largest available radius is smaller than the effective radius R_e, an aperture correction is applied, following the method described in van

de Sande et al. (2017a). The measurements we use have also been corrected for seeing, with the method described in Harborne et al. (2020).

We also make considerable use of $\lambda_{R_e}^{\rm edge-on}$, the λ_{R_e} measurements corrected to an edge-on projection, and hereafter referred to as $\lambda_{R_e}^{\rm eo}$. These values are obtained following the method described in van de Sande et al. (2018) and van de Sande et al. (2021b). They are derived from the observed λ_{R_e} and ϵ_e measurements, assuming theoretical model predictions for galaxies as rotating, oblate spheroids with varying intrinsic shape and anisotropy. No correction is applied (*i.e.* $\lambda_{R_e}^{\rm eo} = \lambda_{R_e}$) for galaxies that are not consistent with being simple rotating spheroids.

3.3 Line fitting

For all linear fits, we make use of the Python library LMFIT by Newville et al. (2020), where we minimize the quantity

$$\chi^2 = \sum_{j=1}^{N} \frac{[a(x_j - x_0) + b - y_j]^2}{(a\Delta x_j)^2 + (\Delta y_j)^2}, \quad (2)$$

adopted from Tremaine et al. (2002), which accounts for errors in both x and y. We set x_0 to zero unless otherwise stated, to simplify comparisons throughout the paper and with other studies. The inclusion of additional terms for intrinsic scatter, or minimizing the scatter orthogonal to the relation, does not change our results.

3.4 Completeness

We make a series of cuts to the overall sample of 3068 unique galaxies in the SAMI Galaxy Survey. In Watson et al. (2022), we established that galaxies at redshifts $z > 0.072$ showed strong signs of skyline contamination, which affected our measurements of [α/Fe]. We therefore reject these galaxies, leaving 2773 galaxies with $z \leq 0.072$, which we take as our baseline for completeness.

We apply the recommended quality cuts from van de Sande et al. (2017b) to the kinematic measurements. These include Q_1, which requires the line-of-sight velocity v to have a maximum uncertainty $v_{\rm error} < 30\,{\rm km\,s^{-1}}$, and Q_2, that the uncertainty on the velocity dispersion σ follows $\sigma_{\rm error} < 0.1\sigma_{\rm obs} + 25\,{\rm km\,s^{-1}}$. The cumulative effect of Q_1 and Q_2 reduces the sample size to 1566 galaxies.

We also apply the quality cuts from Watson et al. (2022). We remove 7 galaxies with a spectral S/N < 20, and 1 galaxy with $\log_{10}(\sigma) < 1.6$. We further remove 20 galaxies which either fall on the outer limits of the parameter space in [α/Fe] or have uncertainties spanning the entire range. This leaves us with 1538 galaxies, with the cumulative effect shown in Fig. 1. We measure the completeness against the 2773 galaxies with $z \leq 0.072$. The culled sample is >80 per cent complete for $\sigma > 70\,{\rm km\,s^{-1}}$, and for $M_r < -21$. The completeness of the sample suffers at low σ, and similarly for the magnitude distribution, we find > 90 per cent of galaxies fainter than $M_r = -18$ are cut.

Since our analysis depends on fitting a reliable relationship between [α/Fe] and σ, we enforce a final cut to our sample. We reject all galaxies with $\log_{10}(\sigma) < 1.75$, such that we have a completeness of >50 per cent throughout the full range of velocity dispersion. The remaining 1492 galaxies are referred to as the 'kinematic sample'. Comparing against the sample of 2093 galaxies used in Watson et al. (2022), we have cut a substantially higher number of galaxies at low velocity dispersion due to the additional constraints from van de Sande et al. (2017b). The number of galaxies of each type are summarized in Table 1, where we can see the effect of the quality cuts on the sample morphology distribution. Galaxies classified as Sc are largely removed from the sample, because they typically have $\log_{10}(\sigma) < 1.75$.

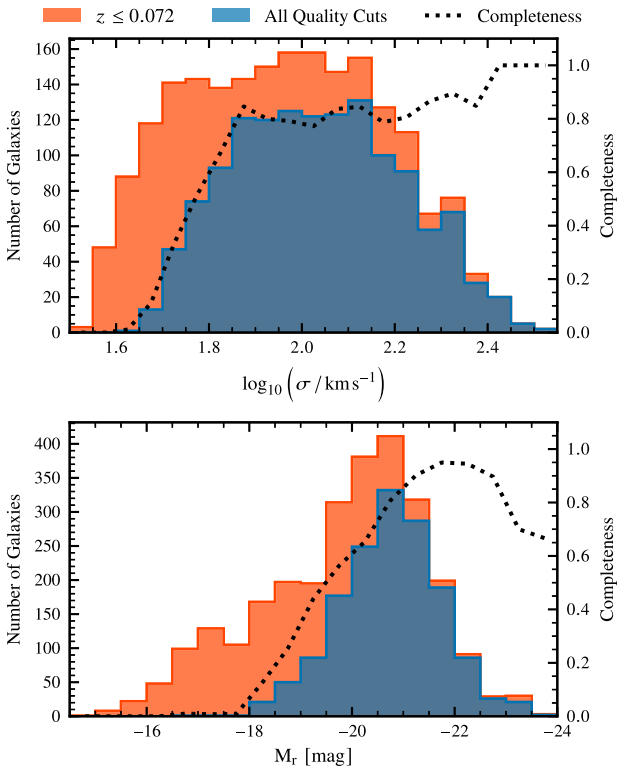

Figure 1. The number of unique galaxies in both the redshift-limited sample, and the core sample after all quality cuts, and their distribution as a function of $\log_{10}(\sigma)$, and absolute magnitude in the r-band, M_r. The dotted line indicates the completeness of our final sample after all quality cuts, relative to the number of unique galaxies with $z \leq 0.072$.

4 RESULTS

4.1 Kinematic classification

We first use the selection criteria from van de Sande et al. (2021a), which have been optimized for use with SGS data. We classify galaxies as SRs if they lie in the region of the λ_{R_e}–ellipticity plane delineated by

$$\lambda_{R_e} < \lambda_{R_{\rm start}} + \epsilon_e/4, \ \text{with} \ \epsilon_e < 0.35 + \frac{\lambda_{R_{\rm start}}}{1.538}, \quad (3)$$

where $\lambda_{R_{\rm start}} = 0.12$. We show this in Fig. 2, noting that our results do not substantially change if we use instead the selection criteria of Cappellari (2016). The remaining galaxies are typically classified as FRs. For our analysis, rather than treating the FRs as a monolithic block, we further subdivide them into four separate groups, sorted by $\lambda_{R_e}^{\rm eo}$ and denoted as Region I–IV, with the selection criteria displayed in Table 1. These criteria were chosen such that a similar range of $\lambda_{R_e}^{\rm eo}$ was surveyed in each group.

4.2 Global relations

We fit a weighted linear relationship between [α/Fe] and $\log_{10}(\sigma)$ to all 1492 galaxies in our final kinematic sample, resulting in $[\alpha/{\rm Fe}] = (0.395 \pm 0.010)\log_{10}(\sigma) - (0.627 \pm 0.002)$. We show the result in Fig. 3, alongside the residuals $\Delta[\alpha/{\rm Fe}]$ as a function of σ.

Table 1. The total number of galaxies used for each stage of the analysis, separated by both optical and kinematic morphology. Intermediate classifications have been grouped with the earlier of the two types, e.g. E/S0 galaxies contribute to the total under the E column. The selection criteria for the kinematic classifications are also shown. These divisions were chosen to give a similar spread of $\lambda_{R_e}^{eo}$ across each Region. Note that Region I does not include galaxies already classified as SRs.

Sample	Total	Optical morphology					Section
		E	S0	Sa/b	Sc	Unclassified	
Unique galaxies	3068	561	728	605	1026	148	
Kinematic sample	1492	323	480	467	191	31	4.1
		Kinematic morphology					
		SR	I	II	III	IV	
$\lambda_{R_e}^{eo}$ Range		equation (3)	≤0.4	0.4–0.525	0.525–0.65	>0.65	
Kinematic sample	1492	121	218	302	432	419	4.1
Quenched sample	657	88	125	196	175	73	4.4

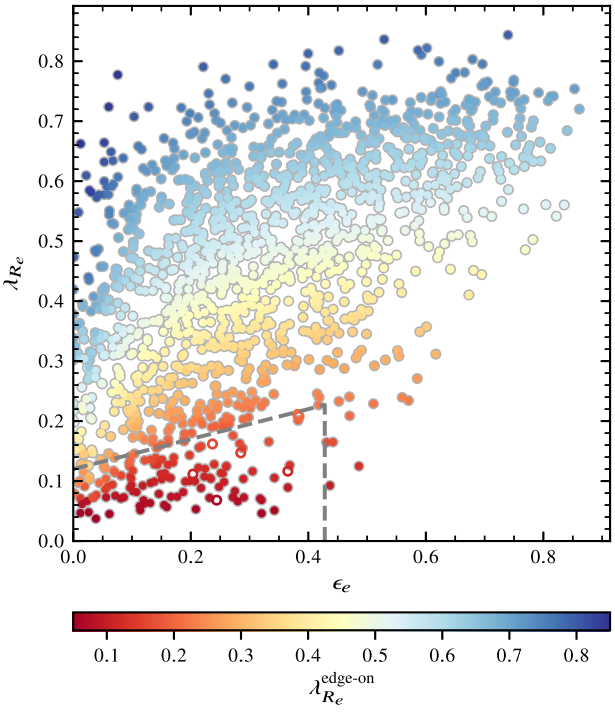

Figure 2. All galaxies in the SGS, for which λ_{R_e} measurements exist, are presented here in the λ_{R_e}–ellipticity plane. Galaxies are coloured according to their $\lambda_{R_e}^{eo}$ values. The dashed line delineates the SR classification from van de Sande et al. (2021a). Open circles represent galaxies which were revealed to be face-on spirals in a visual inspection, and as such are not included in our analysis.

Observing the distribution of the residuals overall, we can see that the scatter decreases with increasing σ, as σ and the spectral S/N are positively correlated across the SGS. Otherwise, there is no underlying structure evident, and the residuals are evenly distributed around 0, as we would expect from the model underlying LMFIT.

In Fig. 3, galaxies are coloured according to their measurements of the inclination-corrected spin proxy $\lambda_{R_e}^{eo}$, using the region classification scheme from Table 1. From this, we can see that there is a clear dependence on $\lambda_{R_e}^{eo}$ in the residuals in Fig. 3b, with Region III and IV galaxies predominantly having $\Delta[\alpha/\text{Fe}] \lessapprox 0$. Conversely, although less pronounced, Region I galaxies are weighted towards higher values of $\Delta[\alpha/\text{Fe}]$.

Therefore, if we instead present the residuals as a function of $\lambda_{R_e}^{eo}$, as in Fig. 3c, we find a statistically-significant anti-correlation. Fitting a linear trendline to this gives the result $\Delta[\alpha/\text{Fe}] = (-0.057 \pm 0.008)\lambda_{R_e}^{eo} + (0.020 \pm 0.004)$. The scatter around this relationship increases slightly towards higher values of $\lambda_{R_e}^{eo}$, although this is not as pronounced as the effect seen in Fig. 3b. If we use the projected values of λ_{R_e} rather than the inclination-corrected $\lambda_{R_e}^{eo}$, the gradient is ∼50 per cent steeper. From Fig. 2, this is the expected outcome of applying the correction, since many galaxies have been shifted to higher numerical values of $\lambda_{R_e}^{eo}$.

4.3 Slow rotators

We also consider the effect of including SRs in this relationship, as they are kinematically distinct from the FRs in the remainder of the sample. We begin by a comparison against galaxies denoted as 'Region I', as discussed in Section 4.1. We show the mass and effective radii distributions of the two groups in Fig. 4. Region I galaxies have a median effective radius of 2.3 kpc, compared to SRs with a median radius of 3.3 kpc. SRs are much rounder than Region I galaxies, with median ellipticities of 0.14 and 0.26 respectively. Similarly, SRs have higher stellar masses, showing a much more sharply peaked distribution with a median stellar mass of $10^{10.9}\,M_\odot$, compared to $10^{10.4}\,M_\odot$ for Region I. This distribution of mass complicates the comparison of [α/Fe] across the two groups. Since we already know that galaxies with higher stellar mass, or velocity dispersion, have a higher α-enhancement on average, we expect the median [α/Fe] of the SRs to be higher. The measured difference of 0.06 dex, whilst significant, is therefore not unexpected.

To make a fair comparison, we instead look at the distribution of the residuals $\Delta[\alpha/\text{Fe}]$, from the global [α/Fe]–σ relation displayed in Fig. 3. The distributions are shown in Fig. 4, and the medians for all regions are given in Table 2. We notice that despite having a higher $[\alpha/\text{Fe}]_{\text{med}}$, the median residual for SRs is almost identical to that of Region I galaxies. Thus, in the region of parameter space where the distributions of galaxy velocity dispersion σ overlap, there is no measurable difference between the [α/Fe] ratio of SRs and Region I galaxies, in contrast to the relation seen across the FRs. We therefore infer that at low $\lambda_{R_e}^{eo}$ ($\lambda_{R_e}^{eo} < 0.4$), any further separation of galaxies by their degree of rotational support, i.e. Region I galaxies and SRs, has no bearing on the [α/Fe] ratio (beyond that arising from the correlation with velocity dispersion), and hence the most probable evolutionary pathway of the stellar component.

The mass and radii distributions for Region I galaxies, shown in Fig. 4, are also consistent with galaxies in Regions II–IV. The median α-enhancement and residual [α/Fe] are given in Table 2.

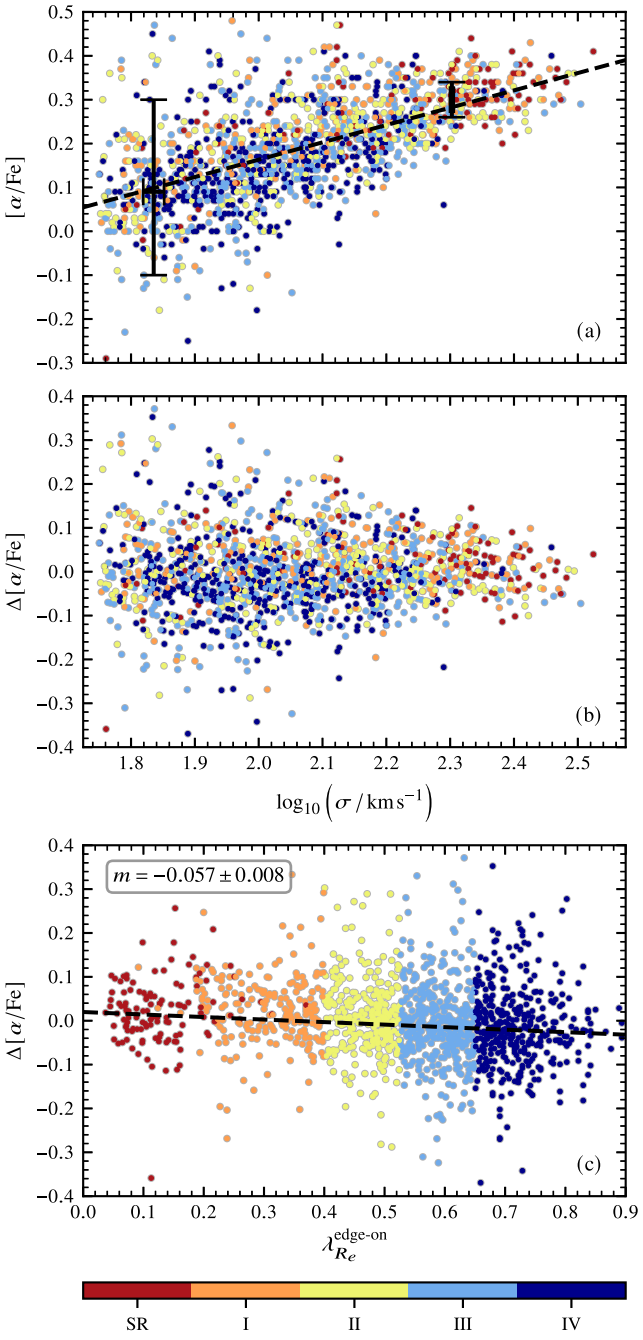

Figure 3. Galaxies are coloured according to their $\lambda_{R_e}^{\mathrm{eo}}$ values, using the region classification scheme from Table 1, with SRs marked in red, and Region IV galaxies in dark blue. The colour scheme is consistent across all four plots. (a) The σ–[α/Fe] relation for our kinematic sample, with the best-fitting linear relation represented by the dashed line. (b) The residuals $\Delta[\alpha/\mathrm{Fe}]$, as a function of $\log_{10}(\sigma)$. There is no correlation, as expected, although the scatter increases at lower values of σ due to the decrease in *S*/*N*. (c) The residuals as a function of $\lambda_{R_e}^{\mathrm{eo}}$. The best-fitting relation is shown as the dashed line, with the gradient m inset.

As we move from $\lambda_{R_e}^{\mathrm{eo}}|_{\mathrm{med}} \sim 0.3$ to higher values, we find that $\Delta[\alpha/\mathrm{Fe}]_{\mathrm{med}}$ decreases monotonically. Taken on its own, this would seem to imply a link between the duration of star formation and the angular momentum of galaxies in Regions I–IV.

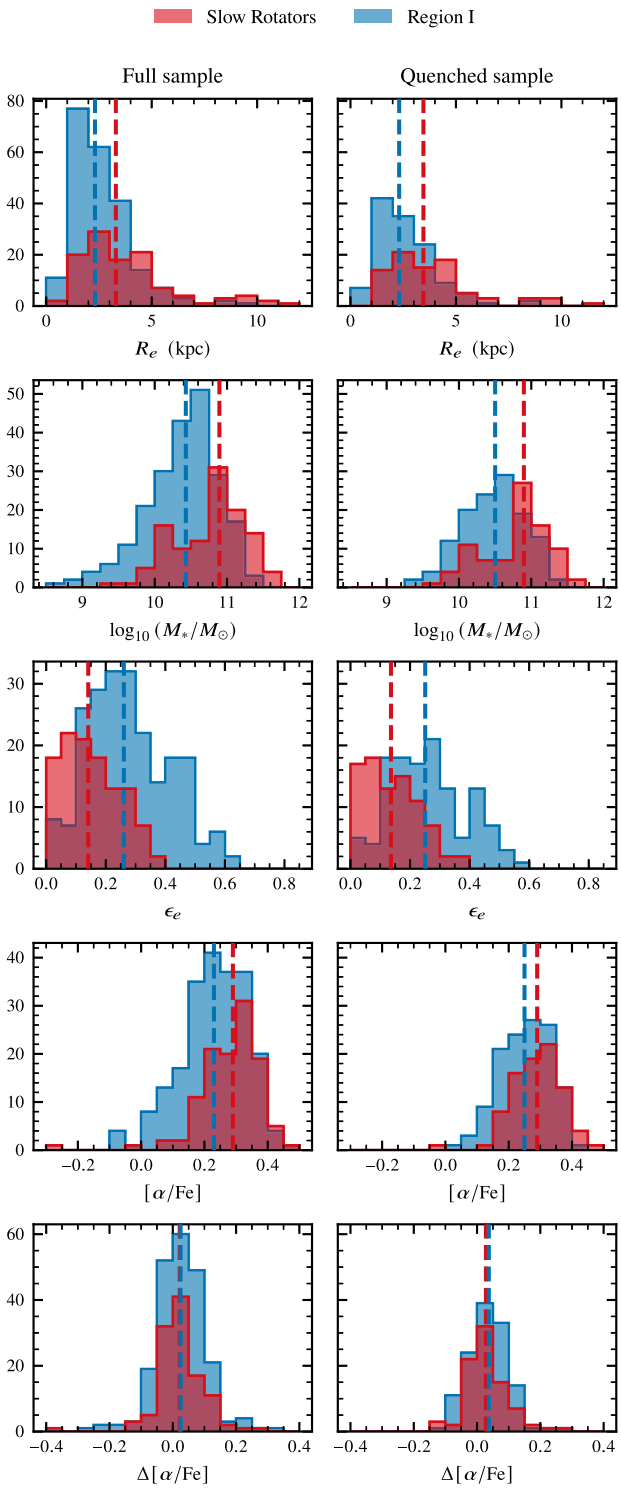

Figure 4. On the left-hand side, we show the difference in the distributions of R_e, $\log_{10}(\mathrm{M}_*/\mathrm{M}_\odot)$, ϵ_e, [α/Fe], and $\Delta[\alpha/\mathrm{Fe}]$ for SRs and Region I galaxies in the full kinematic sample. The dashed lines indicate the medians of each distribution. On the right, we show the same properties after we have isolated the quenched population (see Section 4.4), illustrating that the two populations still show distinct distributions of physical parameters, but no measurable offset in the residual α-enhancement, $\Delta[\alpha/\mathrm{Fe}]$.

Table 2. The median values of $\lambda_{R_e}^{eo}$, [α/Fe] and Δ[α/Fe] for each subsample selected in Section 4.1, where the residuals are measured from the global relation shown in Fig. 3.

Group	$\lambda_{R_e}^{eo}$	[α/Fe]$_{med}$	Δ[α/Fe]$_{med}$
SRs	0.105	0.29	0.022
Region I	0.319	0.23	0.025
Region II	0.483	0.22	0.003
Region III	0.591	0.19	−0.010
Region IV	0.712	0.14	−0.024

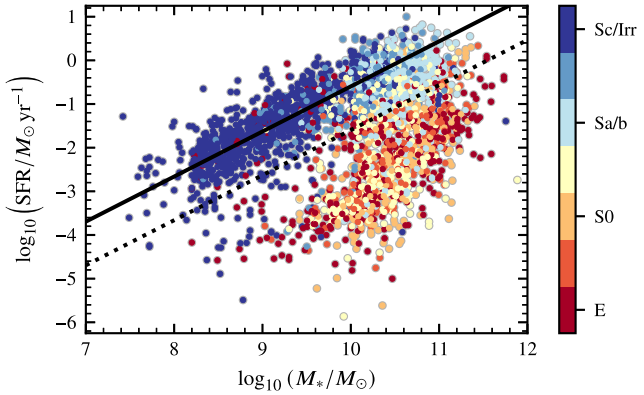

Figure 5. All galaxies in the SGS shown in the SFR-M_* plane. We colour the galaxies according to their optical morphology, and fit the SFMS (denoted as the solid black line) to those classified as Sc/Irr. The dotted black line shows the 1 dex cutoff in SFR, below which we classify galaxies as quenched.

4.4 Relations for the quenched sample

We isolate a quenched subsample of the SGS, utilizing the measurements of the SFR from SAMI DR3. We display all SGS galaxies in the SFR-M$_*$ plane in Fig. 5, where we have colour-coded galaxies by their visual morphology. We select late-type spirals (Sc +) as being the best tracer of the star-forming main sequence (SFMS), in line with previous works such as Medling et al. (2018). We therefore fit the SFMS as a simple linear relationship to the Sc population, using the same procedure as detailed previously in Section 3.3.

From the SFR-M$_*$ plane, we define quenched galaxies as having a SFR more than 1 dex below the SFMS. Despite the arbitrary nature of this threshold, we note that the results in this section are robust against a wide range of selection criteria, even using an offset of just 0.5 dex. We apply the 1 dex selection criteria to our previous $\lambda_{R_e}^{eo}$-based samples, and note that this substantially reduces the sample size available for all our groups, although the effect is not uniform. Region II now consists of 201 galaxies, whilst Region IV contains just 65 galaxies (previously 316 and 430 galaxies respectively). Although this limits our analysis somewhat, it is not unexpected. Galaxies known as 'anaemic spirals', with little ongoing star formation but a visual spiral structure, are known to be only a small fraction of late-type spiral galaxies (van den Bergh 1976).

In light of this, we revisit the comparison of SRs and Region I galaxies established in Section 4.3. In Fig. 4, we compare the structural parameters ($\log_{10}(M_*/M_\odot)$, R_e), and the absolute and residual α-enhancement for the quenched sample. Although there are small shifts in the distributions, and the sample sizes, the overall conclusions are unchanged. SRs are larger and more massive than Region I galaxies, and correspondingly more α-enhanced. As before though, when comparing the residuals Δ[α/Fe] to account for the difference in the mass distributions, we find no such distinction.

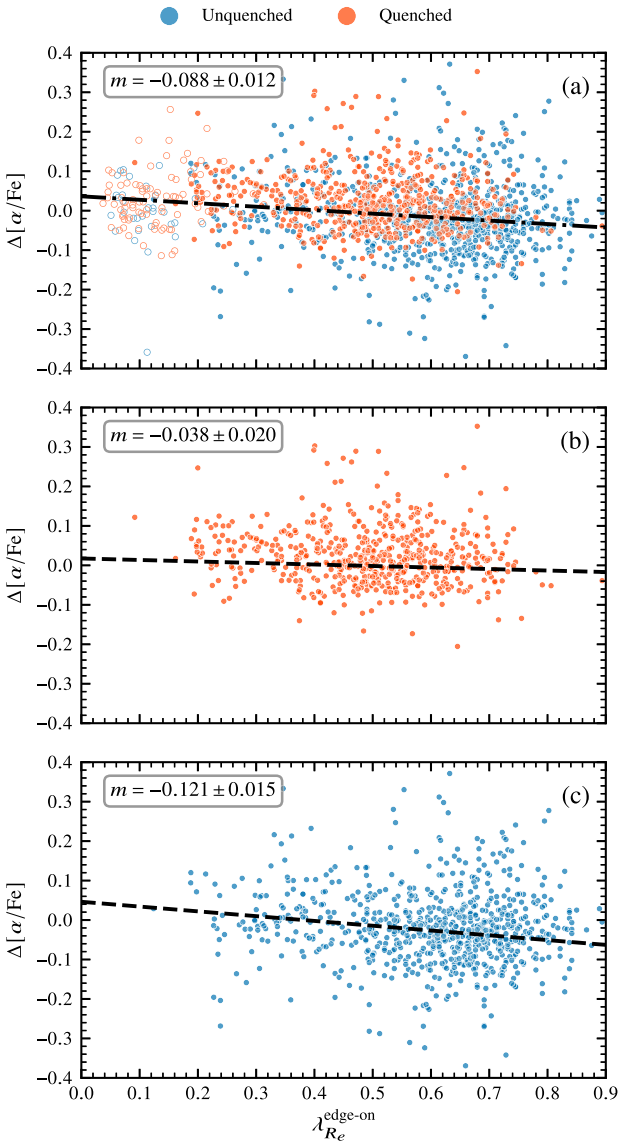

Figure 6. (a) The correlation between the residuals Δ[α/Fe] and $\lambda_{R_e}^{eo}$, using the global [α/Fe]–σ relation from Fig. 3a. The dot-dashed line shows the best-fitting linear relation, with the gradient m inset. Following the discussion in Section 4.3, SRs are not included in the derivation of this relation, but are displayed here as open circles for reference. The galaxies shown are therefore identical to those in Fig. 3c, with a different linear relation. Galaxies are coloured according to their classification as 'quenched' or 'unquenched'. (b, c) As above, but the linear trendlines are fitted only to the quenched and unquenched galaxies respectively.

In fact, quenched Region I galaxies are enhanced by ∼0.01 dex in [α/Fe] compared to SRs, although we do not consider this significant due to the uncertainties on the measurements. These results appear to be consistent with the unquenched sample, although the sample size is too small to draw any firm conclusions.

Considering all classifications, we again analyse the residuals from a global [α/Fe]–σ relationship, shown in Fig. 6. In the top panel, we refit a linear relationship to the residuals, with the SRs excluded from the fit, following the discussion in Section 4.3. In comparison to Fig. 3c, the gradient is ∼50 per cent steeper. Due to the reduction in the sample size, the uncertainty on the fit has also increased, and hence the statistical significance of the relationship is exactly

as before. We note that reusing the fit from Fig. 3a, compared to refitting the [α/Fe]–σ relationship without SRs, has no measurable impact when calculating the residuals, and so this can be excluded as a potential source of bias.

In Fig. 6b, we consider only the quenched galaxies. Comparing to the correlation using the full sample, it is immediately clear that the statistical significance of the Δ[α/Fe]–$\lambda^{eo}_{R_e}$ relation has been substantially reduced.

There are two components to this. Firstly, the sample size has decreased by over a factor of two, from 1492 galaxies to only 657. We therefore expect the uncertainty on our fits to increase, and we note that the ratio of the uncertainties scales with the square root of the sample sizes. Secondly, the removed 'unquenched galaxies' are likely those with ongoing or recent episodes of star formation. As such, we anticipate these galaxies to be substantially less α-enhanced than those in the 'quenched' sample, which would also translate to lower Δ[α/Fe]. By comparing the distribution of galaxies between Figs 6b and 6c, we see that a large proportion of galaxies have been removed from the high $\lambda^{eo}_{R_e}$ regime. The strong gradient for the 'unquenched' galaxies is therefore the clear cause of the flattening of this Δ[α/Fe]-$\lambda^{eo}_{R_e}$ relationship in the 'quenched' sample.

5 DISCUSSION

5.1 Comparisons to previous studies

The multitude of methods of calculating the values of age, metallicity and α-abundance complicate any comparisons of absolute values across different studies. Small changes in the method, such as a different set of stellar population models, can cascade into larger systematic offsets in the final results. Hence, we only consider here the relative trends and scaling relations.

There are few studies directly linking the kinematic morphologies to stellar populations. M15 briefly considered the difference between regular and non-regular rotators (analogous to our Regions I–IV and SRs), and found no significant change in the relative abundance of α-elements. This may be partially caused by the limited distribution of ETGs in the $\lambda^{eo}_{R_e}$-ϵ plane, displayed in Fig. 7 for the SGS. By focussing on ETGs, M15 would have also been limited to a similar sample as in Fig. 6b. This is only a weak relationship, and as such, it is highly likely that any correlation between Δ[α/Fe] and λ_{R_e} would be drowned out by the scatter in the [α/Fe]–σ relation, depending on the sample selection.

Perhaps more relevant is B19, which primarily focused on the radial gradients of galaxies in the MaNGA survey. The selection used by B19 contained almost exclusively ETGs, with the SRs separated by means of a simple cut at $\lambda_{R_e} = 0.2$, rather than the selection criteria first defined by Cappellari (2016) (see Section 4.1 for more details). In each stellar mass and size bin, B19 found offsets of approximately 0.01-0.05 dex in [α/Fe] between fast and SRs, depending on the radial aperture size. This is in broad agreement with our own results, although we note that a similar limitation applies to this as to M15, in that results drawn from a binary kinematic classification are strongly dependent on the distribution of galaxies in the λ_{R_e}-ϵ plane.

To the best of our knowledge, no other work to date has sought to disentangle the relationship between the spin parameter proxy λ_{R_e} and the abundance of α elements, whilst simultaneously mitigating the effects of ongoing star formation, and so we cannot make any further comparisons here.

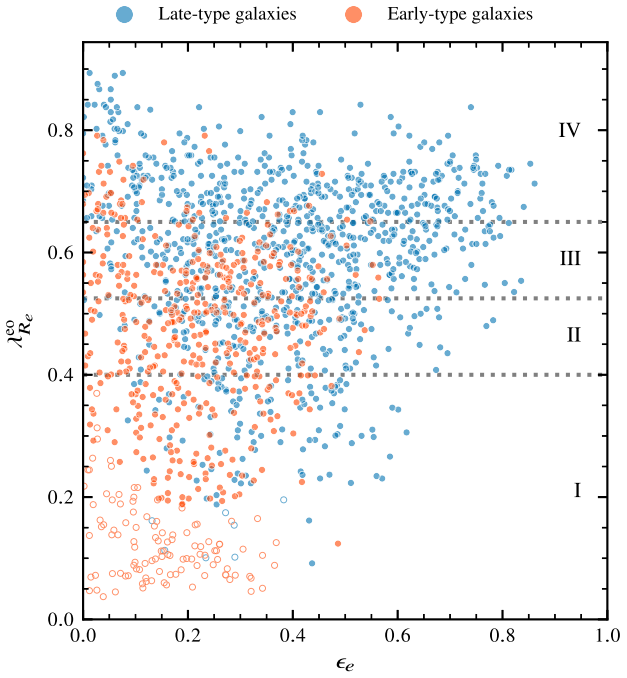

Figure 7. The distribution of SGS galaxies in the $\lambda^{eo}_{R_e}$-ϵ plane, where we have highlighted visually classified ETGs in orange. SRs are represented as open circles, whilst all other galaxies are shown as filled markers. The definitions of Regions I–IV are reproduced from Table 1, and are overlaid as dashed lines.

5.2 Physical implications

In agreement with previous studies, we reproduce the well known relationship between [α/Fe] and σ, which indicates that star formation in massive galaxies was quenched relatively faster than in less massive galaxies.

Analysing residuals from the [α/Fe]–σ relation for the entire sample, we find a statistically significant anti-correlation with the inclination-corrected spin proxy, $\lambda^{eo}_{R_e}$. This indicates that the kinematic structure of a galaxy plays a role in the quenching mechanism, with disc dominated systems having a longer duration of star formation. This is in good agreement with van de Sande et al. (2018), who found an analogous relationship between the luminosity-weighted stellar age, and (V/σ), the ratio of ordered rotation to random motion, although the different quantities measured mean that our results are not directly comparable.

Considering the background in Section 1.1, we suggest that this behaviour is largely consistent with a picture in which classical bulges (CBs) form over considerably shorter periods of time than extended galactic discs. The decrease in the temporal extent of star formation would lead to a relatively higher [α/Fe] in the CB compared to the disc. Considering galaxies at some fixed velocity dispersion, any increase in the bulge-to-disc ratio would correspond to a decrease in the overall rotational support, and hence the measured $\lambda^{eo}_{R_e}$. The relatively larger bulge would produce a greater fraction of the integrated light, and so a global measurement of [α/Fe] would be seen to increase. When taken over a range of velocity dispersion, such a formation scenario would therefore be able to qualitatively explain the observed anti-correlation between $\lambda^{eo}_{R_e}$ and the residuals Δ[α/Fe] shown in Fig. 3.

However, we note that galaxies containing CBs are not likely to account for the majority of our sample. Taking a survey of the local 11 Mpc volume, Fisher & Drory (2011) found only

17 per cent±10 per cent of galaxies had an observed CB, relative to 45 per cent±12 per cent with a pseudo-bulge (PB). This is supported by observational evidence from previous studies in the SGS, with Barsanti et al. (2021) finding 23 per cent of galaxies contained bulges that were older than their discs (probable CBs), and 34 per cent where the bulges were younger (probable PBs). Pseudo-bulges are thought to form out of gas brought to the central regions from the galactic disc, via secular evolution over long time-scales (Athanassoula 2005). In contrast to CBs, which exhibit a wide range of SFRs, PBs are almost universally star-forming (Luo et al. 2020). Integrated over a galaxy, this longer extent of star formation in PBs would suggest a noticeably lower measurement of [α/Fe] compared to CBs. Since PBs do not have substantially different star-formation histories to their surrounding discs, we do not expect the host galaxies to show any clear relationship between their degree of rotational support, and their α-enhancement.

From Fig. 5, we can see that our sample contains a considerable fraction of actively star-forming galaxies. Whilst Luo et al. (2020) demonstrated that CBs themselves have a wide-range of SFRs, a large share of their host galaxies are still star-forming, depending on the morphology and environment (Mishra, Wadadekar & Barway 2019). As such, when investigating the quenched sample, we remove a considerable proportion of galaxies for which we expect $\lambda_{R_e}^{eo}$ and Δ[α/Fe] to be correlated, leading to the relationship displayed in Fig. 6b. By comparison, our unquenched sample most probably consists of a mixture of CBs and PBs. Whilst Fig. 6c demonstrates a clear anti-correlation between the degree of rotational support and α-enhancement, we suggest that the considerable scatter is largely driven by galaxies hosting PBs.

There is considerable support in existing literature for differing quenching mechanisms as a function of kinematic morphology, such as Smethurst et al. (2015). In particular, for disc-dominated galaxies, which would have high $\lambda_{R_e}^{eo}$, Smethurst et al. (2015) found that the dominant quenching mechanisms were those taking place over long time-scales (defined as $\tau > 2$ Gyr). These are likely to be secular processes, i.e. those internal to the galaxy, such as bar formation in spiral galaxies funnelling gas towards central PBs (Cheung et al. 2013). By comparison, the dominant mechanisms for smooth galaxies (those with lower $\lambda_{R_e}^{eo}$) are those taking place over the shortest time-scales ($\tau < 1$ Gyr), such as dry major mergers, perhaps in combination with AGN feedback (Springel, Di Matteo & Hernquist 2005). We would expect the relatively longer quenching time-scales for disc-dominated systems to lead to a lower α-abundance. However, whilst there is some evidence for this in Section 4.4, this is not statistically significant enough for us to draw any firm conclusions. In particular, we cannot conclude whether the observed relationship in Fig. 6b is due to morphological-dependent quenching mechanisms, or a weak residual effect from galaxies containing CBs. We suggest that further study with a larger sample size would be very helpful, especially in order to clarify the statistical significance of this relation. Disentangling the relative contribution of bulges to the overall α-enhancement of galaxies requires a spatially-resolved view, and we intend to explore this effect in more detail in a future paper.

Although there is only weak evidence for this Δ[α/Fe]-$\lambda_{R_e}^{eo}$ relationship persisting in the quenched sample, we show in Fig. 6c that the relationship in the full sample is largely driven by unquenched galaxies. To estimate the physical implications of this result, we can use the empirical formulae of de La Rosa et al. (2011). These were obtained by utilizing full-spectrum fitting in a sample of elliptical galaxies to determine non-parametric star formation histories, and comparing to the abundance ratios derived from line indices, using the same models as we have in this paper (Thomas et al. 2010). One

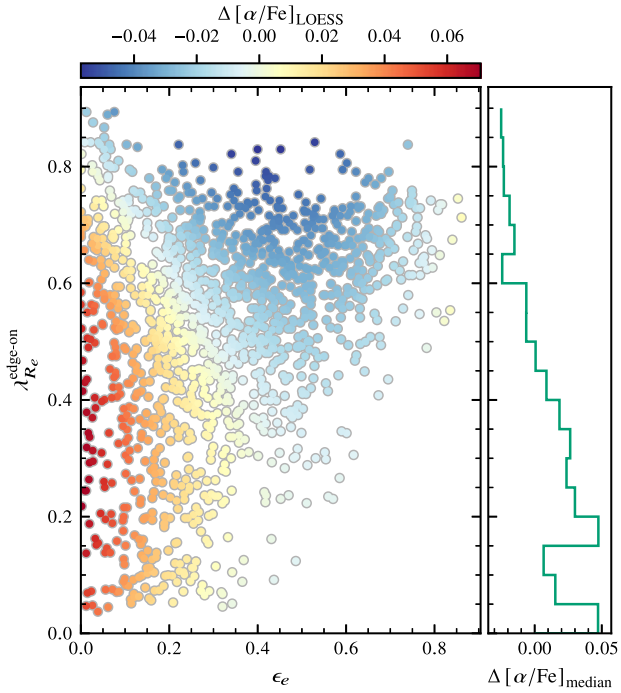

Figure 8. The distribution of SGS galaxies in the $\lambda_{R_e}^{eo}$–ϵ plane. Galaxies are coloured according to their residual α-enhancement, measured relative to the best-fitting relation displayed in Fig. 3. These values have been smoothed using the locally weighted regression technique (LOESS) of Cappellari et al. (2013). The stepped function on the right represents the residuals prior to smoothing, with the median Δ[α/Fe] taken from bins of 0.05 $\lambda_{R_e}^{eo}$.

of these formulae considers the half-mass formation time ($T_{M/2}$) as a function of α-abundance,

$$T_{M/2}(\mathrm{Gyr}) = -15.3[\alpha/\mathrm{Fe}] + 5.2.$$

Looking at the relationship in Fig. 6c, we can therefore predict how $T_{M/2}$ varies at some fixed velocity dispersion,

$$\Delta T_{M/2}(\mathrm{Gyr})\big|_{\rm unquenched} = (-1.85 \pm 0.23)\Delta\lambda_{R_e}^{eo}.$$

As an example, considering the median galaxy in each group, we would expect a Region IV galaxy to have a half-mass formation time ∼0.7 Gyr longer than a galaxy in Region I. To put this in context, at a fixed velocity dispersion of 200 km s^{-1}, considering the global relationship in Fig. 3a, a Region I galaxy would have $T_{M/2} = 0.51$ Gyr, whereas a Region IV galaxy would have $T_{M/2} = 1.26$ Gyr.

Turning our attention to the SRs, the offsets in the distributions in Fig. 4 support the concept that slow and FRs form distinct populations, as far as their structural parameters are concerned. However, we find little evidence for such a binary classification in the stellar populations, with the slow rotators having a residual α-enhancement consistent with Region I galaxies. Considering similar population parameters such as the mean stellar age, we note that studies such as van de Sande et al. (2018) have previously shown a smooth variation of stellar populations across the slow/FR boundary.

Therefore, the unexpected result here is that the residual α-enhancement appears to level off for $\lambda_{R_e}^{eo} < 0.4$. We illustrate this more clearly in Fig. 8, where we show the distribution of residuals in the $\lambda_{R_e}^{eo}$–ϵ plane, after local smoothing using the LOESS algorithm (Cappellari et al. 2013). Whilst there is a clear trend towards lower values of Δ[α/Fe] for $\lambda_{R_e}^{eo} > 0.4$, there is no appreciable difference in the residuals below this point. This may be partially due to the difficulty in determining a clean separation between the two groups.

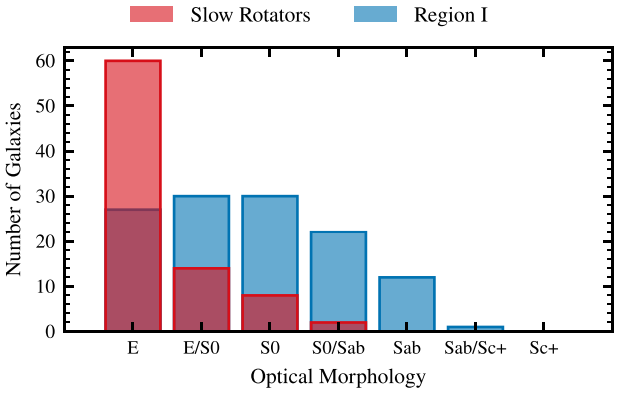

Figure 9. The morphological distribution of SRs and Region I galaxies in our quenched sample. SRs are almost exclusively ellipticals, whereas Region I galaxies show a much more balanced distribution of optical morphologies.

van de Sande et al. (2021a) expands upon this problem of how to accurately determine distinct kinematic classifications in considerable detail, although it is clear that any solution contains a certain degree of compromise. Simplistically, we can see in Fig. 2 the density of galaxies in λ_{R_e}-ϵ space around the cutoff. However, from Fig. 3c, we can also see that the distribution of SRs contains no galaxies substantially higher in $\Delta[\alpha/\mathrm{Fe}]$ than those in Region I. This cannot be changed by altering $\lambda_{R_{\mathrm{start}}}$ or the gradient of the dividing line, and so we reject this selection effect as the driver behind our results.

An additional factor that must be considered is that the SAMI sample is known to contain a non-zero number of galaxies with counter-rotating discs (Rawlings et al. 2020), also referred to as 2σ galaxies. When integrated over a wide enough aperture, these will have a low measured spin proxy due to the summation of the separate disc components, and may be misidentified as SRs. Although most of these galaxies have $\epsilon > 0.4$, and would be caught by the selection criteria introduced in Cappellari (2016), we cannot rule out that this may influence the exact relationship.

As before for the general anti-correlation described in Fig. 3, the similarity between the residual α-enhancement distributions of SRs and Region I galaxies cannot be easily attributed to differing stellar populations across bulge and disc components. Whilst there are bulge-disc decompositions for the SGS, these have been limited so far to subsamples, such as the lenticular cluster sample explored in Barsanti et al. (2021) and the GAMA regions in Lah *et al.* (in prep.), or with stringent quality cuts (Oh et al. 2020). We instead look at the optical morphological classifications of Cortese et al. (2016), presented in Fig. 9 for our quenched sample. Whilst SRs are heavily bulge-dominated systems, with ∼two-thirds unambiguously classified as ellipticals, Region I galaxies show a much greater variation in their morphological classifications. This is in line with the other structural parameters explored in Fig. 4. Hence, despite the limitations discussed previously, we maintain that the similar residual α-enhancement of SRs and Region I galaxies in our sample is a real phenomenon, and one that we hope can be replicated across other spectroscopic surveys.

To explain the likely reasons behind this phenomenon, we explore the SR formation scenarios espoused by Naab et al. (2014). Using a slightly different selection criteria, we see that there are two likely pathways that agree with observations:

(i) Class C: Late ($z \lesssim 1$), gas-rich major mergers. The high fraction of stars formed in the galaxy, relative to those accreted through a merger, would likely result in a low integrated [α/Fe] ratio.

(ii) Class F: Repeated minor mergers, from at least $z \sim 2$. These would likely have significantly higher [α/Fe] than Class C galaxies.

We can see already that the two formation scenarios would likely result in a broad spread of [α/Fe] relative to FRs, and consider the possible mix of Class C and F galaxies as the most probable cause for SRs not following the residual anti-correlation between $\Delta[\alpha/\mathrm{Fe}]$ and $\lambda^{\mathrm{eo}}_{R_e}$. We further speculate that under the formation pathway of Class F galaxies, a recent minor merger with a late-type galaxy may also depress the integrated [α/Fe] ratio, and result in measurements closer to solar values. In addition, the sample used by Naab et al. (2014) predicts both an increase in the median stellar mass and radius of SRs relative to FRs, in good agreement with our results from Fig. 4.

More recently, these results have been reinforced by Lagos et al. (2022), who investigated SR formation scenarios in the EAGLE simulation. They explicitly computed the expected chemical abundances for each assembly history, as a function of galaxy radius. All SRs that formed via mergers were α-enhanced, relative to main sequence galaxies, whereas those that formed without mergers, and hence had little disruption to ongoing star formation, were predicted to have considerably lower [α/Fe] towards the centre. Similarly, investigating SRs that have had any merger in the last 10 Gyrs, those with gas-rich mergers were ∼0.1 dex lower in [α/Fe] than the average, in agreement with the expectations from Naab et al. (2014). Both the 'no merger' and 'gas-rich merger' scenarios could explain the comparable residual α-enhancement of SRs to Region I galaxies. Further work on this area is clearly needed however, as the spatial information in the kinematic maps may be able to reveal which formation pathway is dominant in this sample.

6 CONCLUSIONS

We utilize measurements of [α/Fe] from Watson et al. (2022) and $\lambda^{\mathrm{eo}}_{R_e}$ from van de Sande et al. (2021a) to analyse galaxies in the SAMI Galaxy Survey. Based on our analysis of the kinematic properties across the sample, we make the following observations:

(i) For all 1492 galaxies with measurements of λ_{R_e}, we fit a global [α/Fe]–σ relation to obtain the result

$$[\alpha/\mathrm{Fe}] = (0.395 \pm 0.010)\log_{10}(\sigma) - (0.627 \pm 0.002).$$

We find that the residuals $\Delta[\alpha/\mathrm{Fe}]$ display a strong anti-correlation with the inclination corrected $\lambda^{\mathrm{eo}}_{R_e}$,

$$\Delta[\alpha/\mathrm{Fe}] = (-0.057 \pm 0.008)\lambda^{\mathrm{eo}}_{R_e} + (0.020 \pm 0.003).$$

If we use λ_{R_e} rather than $\lambda^{\mathrm{eo}}_{R_e}$, the gradient of the correlation is over 50 per cent higher.

(ii) We isolate the quenched population based on a 1 dex offset in star formation rate from the star-forming main sequence. This substantially reduces the statistical significance of this anti-correlation, which now has a gradient $m = -0.038 \pm 0.020$. However, the persistence of this relation, whilst weak, demonstrates that the offset cannot unambiguously be attributed to ongoing star formation.

(iii) Unquenched galaxies demonstrate a much more significant relationship,

$$\Delta[\alpha/\mathrm{Fe}] = (-0.121 \pm 0.015)\lambda^{\mathrm{eo}}_{R_e} + (0.046 \pm 0.009).$$

(iv) This anti-correlation would therefore imply a link between the duration of star formation and the angular momentum of the galaxy. Utilizing the empirical formulae of de La Rosa et al. (2011), we estimate the half-mass formation time of unquenched galaxies in Region IV to be extended by ∼0.7 Gyr relative to those in Region I.

$$\Delta T_{\mathrm{M/2}}(\mathrm{Gyr}) = (-1.85 \pm 0.23)\Delta\lambda^{\mathrm{eo}}_{R_e}. \quad (4)$$

We hope to further explore this link in future studies.

(v) Comparing SRs to the lowest $\lambda_{R_e}^{eo}$ FRs (Region I), we find that the difference in α-enhancement is determined to first order by σ. Accounting for this, by looking at the residuals $\Delta[\alpha/\mathrm{Fe}]$, we find the SRs and Region I galaxies are indistinguishable. The star formation histories of these two groups ($\lambda_{R_e}^{eo} \lessapprox 0.4$) are therefore similar, despite a substantial difference in their structure and kinematics. This contrasts with galaxies in Regions II–IV, which show increasingly extended star formation histories, correlated with their degree of rotational support.

ACKNOWLEDGEMENTS

The SAMI Galaxy Survey is based on observations made at the AAT, and was developed jointly by the University of Sydney and the Australian Astronomical Observatory. The SAMI input catalog is based on data taken from the Sloan Digital Sky Survey, the GAMA Survey, and the VST ATLAS Survey. The SAMI Galaxy Survey is supported by the Australian Research Council Centre of Excellence for All Sky Astrophysics in 3 Dimensions (ASTRO 3D), through project number CE170100013, the Australian Research Council Centre of Excellence for All-sky Astrophysics (CAASTRO), through project number CE110001020, and other participating institutions. The SAMI Galaxy Survey website is http://sami-survey.org/.

PJW and RLD acknowledge travel and computer grants from Christ Church, Oxford, and support from the Oxford Hintze Centre for Astrophysical Surveys which is funded by the Hintze Family Charitable Foundation. RLD is also supported by the Science and Technology Facilities Council grant numbers ST/H002456/1, ST/K00106X/1, and ST/J002216/1. JvdS acknowledges support of an Australian Research Council Discovery Early Career Research Award (DE200100461) funded by the Australian Government. SB acknowledges funding support from the Australian Research Council through a Future Fellowship (FT140101166). FDE acknowledges funding through the ERC Advanced grant 695671 'QUENCH', the Horizon 2020 European Research Council consolidator grant 683184 and support by the Science and Technology Facilities Council. BG is the recipient of an Australian Research Council Future Fellowship (FT140101202). NS acknowledges support of an Australian Research Council Discovery Early Career Research Award (DE190100375) funded by the Australian Government and a University of Sydney Postdoctoral Research Fellowship. JBH is supported by an Australian Research Council Laureate Fellowship (FL140100278). The SAMI instrument was funded by Bland-Hawthorn's former Federation Fellowship (FF0776384), an Australian Research Council Linkage Infrastructure, Equipment and Facilities grant (LE130100198; PI Bland-Hawthorn) and funding from the Anglo-Australian Observatory. JJB acknowledges support of an Australian Research Council Future Fellowship (FT180100231). MSO acknowledges funding support from the Australian Research Council through a Future Fellowship (FT140100255).

DATA AVAILABILITY

All data used in this work are publicly available from Astronomical Optics' Data Central service at https://datacentral.org.au/ as part of the SAMI Data Release 3 (Croom et al. 2021).

REFERENCES

Ahn C. P. et al., 2012, ApJS, 203, 21
Allen J. T. et al., 2015, MNRAS, 446, 1567
Annibali F., Grützbauch R., Rampazzo R., Bressan A., Zeilinger W. W., 2011, A&A, 528, A19
Athanassoula E., 2005, MNRAS, 358, 1477
Barsanti S. et al., 2021, ApJ, 906, 100
Bender R., Burstein D., Faber S. M., 1992, ApJ, 399, 462
Bernardi M., Domínguez Sánchez H., Brownstein J. R., Drory N., Sheth R. K., 2019, MNRAS, 489, 5633
Bland-Hawthorn J. et al., 2011, Opt. Express, 19, 2649
Bryant J. J., Bland-Hawthorn J., Fogarty L. M. R., Lawrence J. S., Croom S. M., 2014, MNRAS, 438, 869
Bryant J. J. et al., 2015, MNRAS, 447, 2857
Bundy K. et al., 2015, ApJ, 798, 7
Cappellari M., 2002, MNRAS, 333, 400
Cappellari M., 2016, ARA&A, 54, 597
Cappellari M., 2017, MNRAS, 466, 798
Cappellari M. et al., 2011, MNRAS, 413, 813
Cappellari M. et al., 2013, MNRAS, 432, 1862
Cenarro A. J., Cardiel N., Gorgas J., Peletier R. F., Vazdekis A., Prada F., 2001, MNRAS, 326, 959
Chabrier G., 2003, PASP, 115, 763
Cheung E. et al., 2013, ApJ, 779, 162
Cortese L. et al., 2016, MNRAS, 463, 170
Croom S. M. et al., 2012, MNRAS, 421, 872
Croom S. M. et al., 2021, MNRAS, 505, 991
D'Eugenio F. et al., 2021, MNRAS, 504, 5098
Davies R. L., Sadler E. M., Peletier R. F., 1993, MNRAS, 262, 650
de La Rosa I. G., La Barbera F., Ferreras I., de Carvalho R. R., 2011, MNRAS, 418, L74
de Zeeuw P. T. et al., 2002, MNRAS, 329, 513
Driver S. P. et al., 2011, MNRAS, 413, 971
Eggen O. J., Lynden-Bell D., Sandage A. R., 1962, ApJ, 136, 748
Emsellem E., Monnet G., Bacon R., 1994, A&A, 285, 723
Emsellem E. et al., 2007, MNRAS, 379, 401
Emsellem E. et al., 2011, MNRAS, 414, 888
Falcón-Barroso J., Sánchez-Blázquez P., Vazdekis A., Ricciardelli E., Cardiel N., Cenarro A. J., Gorgas J., Peletier R. F., 2011, A&A, 532, A95
Fisher D. B., Drory N., 2011, ApJ, 733, L47
Franx M., Illingworth G., 1990, ApJ, 359, L41
Graham M. T. et al., 2018, MNRAS, 477, 4711
Green A. W. et al., 2018, MNRAS, 475, 716
Greggio L., Renzini A., 1983, A&A, 118, 217
Harborne K. E., van de Sande J., Cortese L., Power C., Robotham A. S. G., Lagos C. D. P., Croom S., 2020, MNRAS, 497, 2018
Kennicutt Robert C. J., Tamblyn P., Congdon C. E., 1994, ApJ, 435, 22
Krajnović D. et al., 2011, MNRAS, 414, 2923
Krajnović D. et al., 2020, A&A, 635, A129
Lagos C. d. P., Emsellem E., van de Sande J., Harborne K. E., Cortese L., Davison T., Foster C., Wright R. J., 2022, MNRAS, 509, 4372
Larson R. B., 1974, MNRAS, 166, 585
Luo Y. et al., 2020, MNRAS, 493, 1686
McDermid R. M. et al., 2015, MNRAS, 448, 3484
Medling A. M. et al., 2018, MNRAS, 475, 5194
Mishra P. K., Wadadekar Y., Barway S., 2019, MNRAS, 487, 5572
Naab T. et al., 2014, MNRAS, 444, 3357
Newville M. et al., 2020, lmfit/lmfit-py 1.0.1. Available at: https://doi.org/10.5281/zenodo.3814709
Oh S. et al., 2020, MNRAS, 495, 4638
Oke J. B., Gunn J. E., 1983, ApJ, 266, 713
Owers M. S. et al., 2017, MNRAS, 468, 1824
Proctor R. N., Forbes D. A., Beasley M. A., 2004, MNRAS, 355, 1327
Rawlings A. et al., 2020, MNRAS, 491, 324
Sánchez S. F. et al., 2012, A&A, 538, A8
Sánchez S. F. et al., 2021, A&A, 652, L10
Saunders W. et al., 2004, in Moorwood A. F. M., Iye M., eds, Proc. SPIE Conf. Ser. Vol. 5492, Ground-based Instrumentation for Astronomy. SPIE, Bellingham, p. 389
Scott N. et al., 2017, MNRAS, 472, 2833

Scott N. et al., 2018, MNRAS, 481, 2299
Segers M. C., Schaye J., Bower R. G., Crain R. A., Schaller M., Theuns T., 2016, MNRAS, 461, L102
Shanks T. et al., 2013, The Messenger, 154, 38
Shanks T. et al., 2015, MNRAS, 451, 4238
Sharp R. et al., 2006, in Proc. SPIE Conf. Ser. Vol. 6269, Ground-based and Airborne Instrumentation for Astronomy. SPIE, Bellingham, p. 62690G
Slipher V. M., 1914, Lowell Observatory Bulletin, 2, 66
Smethurst R. J. et al., 2015, MNRAS, 450, 435
Smith G. A. et al., 2004, in Moorwood A. F. M., Iye M., eds, Proc. SPIE Conf. Ser. Vol. 7015 5492, Ground-based Instrumentation for Astronomy. SPIE, Bellingham, p. 410
Springel V., Di Matteo T., Hernquist L., 2005, ApJ, 620, L79
Taylor E. N. et al., 2011, MNRAS, 418, 1587
Thomas D., Maraston C., Schawinski K., Sarzi M., Silk J., 2010, MNRAS, 404, 1775
Trager S. C., Worthey G., Faber S. M., Burstein D., González J. J., 1998, ApJS, 116, 1
Trager S. C., Faber S. M., Worthey G., González J. J., 2000, AJ, 120, 165
Tremaine S. et al., 2002, ApJ, 574, 740
van de Sande J. et al., 2017a, MNRAS, 472, 1272
van de Sande J. et al., 2017b, ApJ, 835, 104
van de Sande J. et al., 2018, Nature Astron., 2, 483
van de Sande J. et al., 2021a, MNRAS, 505, 3078
van de Sande J. et al., 2021b, MNRAS, 508, 2307
van den Bergh S., 1976, ApJ, 206, 883
Watson P. J. et al., 2022, MNRAS, 510, 1541
Worthey G., Ottaviani D. L., 1997, ApJS, 111, 377

This paper has been typeset from a TEX/LATEX file prepared by the author.